



# Scintillating anticoincidence detection elements design and tests with muons and protons

M. Gilliot <sup>a,\*</sup>, J. Chabaud <sup>a</sup>, J.P. Baronick <sup>a</sup>, S. Colonges <sup>a</sup>, P. Laurent <sup>a,b</sup>

<sup>a</sup> Laboratoire APC, AstroParticules & Cosmologie, Bâtiment Condorcet, 10 rue Alice Domont et Léonie Duquet, 75205 Paris Cedex 13, France

<sup>b</sup> CEA/DSM/Irfu/SaP, CEA/Saclay, 91191 Gif-Sur-Yvette Cedex, France

## ARTICLE INFO

### Article history:

Received 30 April 2010

Accepted 1 June 2010

Available online 8 June 2010

### Keywords:

Anticoincidence

Muon telescope

Photomultiplier

Scintillator

Simbol-X

## ABSTRACT

Design, construction and tests of anticoincidence detection elements are presented. Initially planned to be used as active shielding parts of the anticoincidence detector of the Simbol-X mission, they are aimed to detect cosmic protons and provide veto signal against charged-particle background induced on imaging detectors. The sample is made of a scintillator plate into which grooves are machined and waveshifting fibers glued. The fibers are connected to multianode photomultiplier (PM) tubes. The tubes characteristics have been evaluated for this application. The device has been tested with atmospheric muons that deposit similar energy to that of cosmic protons thanks to a specially designed muon telescope also described in this paper. Tests have also been performed with protons of a tandem accelerator beam line. The response is on average above 10 photoelectrons, which is not complicated to detect, which allows very good detection efficiency as well as very good ability to reject noise. In addition many evolution and performance improvements appear possible.

© 2010 Elsevier B.V. All rights reserved.

## 1. Introduction

Simbol-X is a high energy astrophysics mission project dedicated to hard X-ray imaging and spectroscopy in the  $\sim 0.5$ – $80$  keV X-ray range with two main science objectives: black hole physics and census, and particle acceleration mechanisms. The instrument would be able to observe a great variety of astrophysical sources with various observation time for a planned schedule of 500 observations per year. It is characterized by high angular resolution and submicro-Crab sensitivity offered by the use of grazing incidence optics and imaging detectors in a very long focal length telescope (20 m), which should provide several orders of magnitude improvement. To achieve this long focal length, the instrument is distributed into two spacecrafts (mirror spacecraft and detector spacecraft) in a formation flying configuration. The mirror spacecraft is on natural orbit while the detector spacecraft is slaved in position with respect to the telescope axis. The relative positioning accuracy needs to be better than 1 cm in all directions while a post-processing absolute pointing reconstruction is operated, based on the knowledge of the relative positions of the two spacecrafts at the 0.5 mm level. More details are given in the 2nd international Simbol-X symposium proceedings [1].

The telescope consists of a classical Wolter I optics with multi-layer mirror technology focussing X-rays onto a focal plane

detection system composed of two superposed detectors of  $128 \times 128$  pixels covering angular size of  $\sim 6.4 \times 6.4$  arcsec<sup>2</sup>. The Simbol-X focal plane installed on the detector spacecraft is designed to detect photons focused by the mirror spacecraft in the 0.5–80 keV energy band and will measure the position, energy, and arrival time of each incoming X-ray photon. It is composed of a low energy detector (0.5–20 keV) and a high energy imaging detector (5–80 keV) on top of each other (Fig. 1). The low energy detector is silicon-based and has already reached an energy resolution of 130 eV at 6 keV for an operating temperature of  $-40$  °C. The high-energy detector is a hard X-ray camera made of arrays of  $8 \times 8$  ‘Caliste’ modules made of 2 mm thick CdTe crystals, each module being divided into an array of  $16 \times 16$  pixels. At this stage of the project, the Caliste module has already obtained a 0.78 keV resolution at 60 keV, well within the Simbol-X specification.

The scientific performances of the Simbol-X mission require a very low detector background level, which involves efficient background rejection systems. Two types of incoming radiation should especially be taken into account: cosmic protons in the  $\sim 1$  GeV energy range with expected count rate of  $\sim 2$  s<sup>-1</sup> cm<sup>-2</sup>, and cosmic photons in the  $\sim 1$ – $10^6$  keV energy range with expected count rate of  $\sim 200$  s<sup>-1</sup> cm<sup>-2</sup>. A collimator should be placed on top to shield all photons not coming from the mirror field of view whereas the whole detectors system should be surrounded by the anticoincidence shielding to remove the background induced by high energy photons and particles running through the satellite. The required efficiency of the anticoincidence 99% detection of the  $\sim 5000$  s<sup>-1</sup> charged particles

\* Corresponding author.

E-mail address: [mickael.gilliot@univ-reims.fr](mailto:mickael.gilliot@univ-reims.fr) (M. Gilliot).

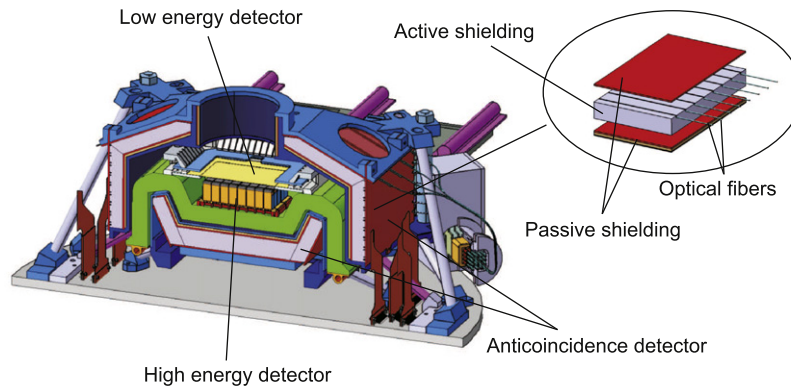


Fig. 1. Focal plane view with zoom on the active and passive shieldings.

on the whole antineutrino and 99.9% stopping of the  $\sim 0.5\text{--}80\text{ keV}$  background photons while not inducing fluorescence emission higher than  $10^{-5}\text{ s}^{-1}\text{ cm}^{-2}\text{ keV}^{-1}$  in the two detectors. Due to integration constraints, the antineutrino assembly is divided into two parts, the upper and the lower antineutrino, each of these parts being, respectively, composed of 8 and 5 tiles. Each tile is made of two layers: a passive shielding to stop photons and an active shielding to detect charged particles and provide a fast veto signal to the imaging detectors. The passive shielding is a sandwich of different metals: a single layer of tantalum on the outside of the active shielding to stop high energy photons and a graded shield on the other side (successive layers of tin, copper, aluminium and carbon) to remove the shield fluorescence (Fig. 1). The active shielding is made with plastic scintillator tiles with wavelength shifting optical fibers glued into grooves (Fig. 1). The fibers in number of eight per tile (plus eight redundant fibers) collect the light generated into the scintillator and direct the photons to photomultiplier tubes (PMTs) to provide an electrical information. All fibers are four by four grouped together and each group connected to pixels of a multianode PM.

This technique consisting in using embedded fibers allows having the PMs away from the scintillators. Many different parameters such as fiber numbers and spacing, fiber type and size, scintillator type, grooves shape, wrapping, fiber termination can be optimized to get the required detection level [2]. It has already been used many times in ground experiments [3] especially in configuration of reading by multianode PMs [4–7] but has very seldom been used in space missions. Plastic scintillator detector with wavelength-shifting fiber in grooves have been used in GLAST/FERMI gamma-ray telescope with different geometry conditions [8,9]. Multiclad scintillating optical fiber assemblies glued on the sides of scintillators have also been used in Agile gamma-ray observation satellite [10]. Such an antineutrino has, however, never been used with low-energy X-ray detector. In the paper we present first results obtained on a prototype piece of active shielding made of scintillator, fibers inserted and connection to multianode PM and show the potential of this technique for use in space missions such as Simbol-X. The main elements of this active shielding, namely PMs and scintillator/fiber assembly, have been reviewed. To achieve this a Hamamatsu R5900 multianode PM has been studied and calibrated in details and then a sample of active shielding has been built and tested. To test this prototype, a specially designed muon telescope has been used. The device has also been tested using 15–20 MeV protons of a tandem accelerator beam line. In the paper details about the muon telescope elaboration are first given, then PMs calibration and response characteristics are presented, and finally the fabrication process and the response of muons and protons are given.

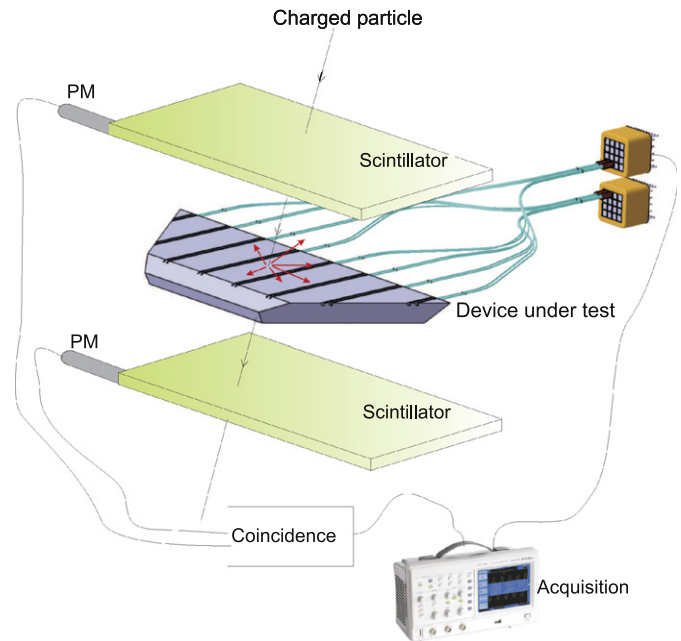


Fig. 2. Muon telescope principle.

## 2. Muon telescope

Muon telescopes are devices capable of detecting particles hitting the Earth surface, produced by the interaction of cosmic radiation with the atmosphere. We have developed a telescope to detect muons in the GeV order of energy and use them as excitation particles to characterize our scintillator-based devices. Prior to using it, the telescope has to be calibrated into different steps: calibration of PMs, calibration of paddles and coincidence control.

### 2.1. Design

Our muon telescope is basically made of two scintillator plates. A schematic view is given in Fig. 2. Light emitted when a particle runs through the scintillator is partly coupled to a wavelength shifter bar glued on it and directed to a PM. A coincidence is done between the two paddles (we refer as paddle the set of a scintillation plate, a wavelength shifting bar and a PM) which emits a trig signal when a particle is detected running through both paddles. The device to be characterized is placed between these two paddles. The scintillator planes are  $350 \times 350$

$\times 10 \text{ mm}^3$  Saint-Gobain Crystal BC-400; the wavelength shifter bar is  $400 \times 10 \times 10 \text{ mm}^3$  Eljen EJ-280. They are glued together with Saint-Gobain Crystal BC-600 optical cement. At the end of the bar a Photonis XP 3102 PM is used to detect light coupled from scintillator to the shifting bar. The link between the shifting material and PM entrance window is made thanks to a BC-634A Saint-Gobain silicone optical interface disk. Finally the plates are wrapped with an aluminium paper sheet so that no light produced in the scintillator can escape and produce parasitic light to the other components. All the two paddles and device to be tested are placed on the different stages of a shelf sheltered from surrounding light.

## 2.2. Photodetection

When a photon strikes the cathode of the PM, it has a probability to produce an electron. If such a photoelectron is created, it is accelerated and multiplied so that an electrical signal can be observed on a resistor placed on the output of the PM. Calibration of the PMs aims to evaluate characteristics of the output signal when 1 photoelectron is produced at the photocathode level. This then gives the charge gain of the PMs which, according to linearity property response of PMs, allows to determine the number of photoelectrons corresponding to any output signal. To achieve the single photoelectron configuration signal the PM is placed in a box in which a very low light level is introduced with intensity not higher than a few thousands of events per second at the output of the PM so that we are confident to be in the single photoelectron regime. Note that once a PM is introduced into the box, it is left a few hours unpowered and unused so that it can restore from potential previous ambient illumination.

The calibration process consists then in making acquisition of a large number of these single photoelectron output signals (typically 10 000 output pulses) and to process them statistically to extract characteristics such as average amplitude and electrical charge. Our experimental treats the pulses at the output of the PM in three steps: amplification, discrimination and acquisition. The signal is acquired and analyzed by a LeCroy WaveRunner 64xi oscilloscope with large bandwidth which can measure parameters such as amplitude and electrical charge (by integration of the voltage signal over the temporal window of observation) at the same time and correlate them. Its input signal are the output signals of the PM through a  $50 \Omega$  load resistor with  $20 \times$  amplification. It is negative voltage with a few tens mVs of amplitude. Before acquisition the input (amplified) signals are discriminated by triggering the oscilloscope on a selected negative voltage level. This level is referred in the text as the discrimination level which acts as a filter level to select only pulses with amplitude above the selected voltage level.

Two Photonis XP 3102 PMs attached to VD101T/A assemblies including voltage divider have been characterized with this setup. After having carefully chosen the discrimination voltage level to filter the main part of noise signals, amplitude and electrical charges of 10 000 consecutive output pulses have been measured when the PMs are powered with a  $-1000 \text{ V}$  negative polarity mode. The mean charge of the single photoelectron response is evaluated to  $-4.9 \times 10^{-13}$  and  $-5.1 \times 10^{-13} \text{ C}$ , which corresponds to gains in number of electrons of  $3 \cdot 10^6$  and  $3.2 \times 10^6$  for the two PMs and mean amplitude of  $130 \text{ mV}$  for both PMs.

The dark current characteristics of these PMs has then been investigated by putting them in total darkness. Dark current pulses are pulses initiated by electrons generated by other processes than photonic excitation. They have to be managed to avoid generating false trig events. The dark current pulses average

**Table 1**

Characteristics of the two PMs used in the muon telescope.

Discr. (mV)	PM1			PM2		
	Rate ( $\text{s}^{-1}$ )	Ampl. (mV)	Charge ( $\text{n pe}^{-}$ )	Rate ( $\text{s}^{-1}$ )	Ampl. (mV)	Charge ( $\text{n pe}^{-}$ )
–20	107.0	–142	1.3	94.5	–131	1.1
–40	92.3	–155	1.4	77.9	–146	1.3
–60	77.6	–168	1.5	63.8	–161	1.4
–80	61.2	–185	1.7	47.0	–179	1.6
–100	46.9	–203	1.8	36.2	–197	1.8
–150	12.2	–318	3.7	10.0	–293	3.1
–250	2.8	–774	9.9	1.9	–733	9.1

The average charge is given in number of electrons and also in corresponding equivalent number of photoelectrons produced at the photocathode.

**Table 2**

Noise characteristics of the two paddles used in the muon telescope as a function of the discrimination level.

Discr. (mV)	Paddle 1			Paddle 2		
	Rate ( $\text{s}^{-1}$ )	Charge ( $\text{n pe}^{-}$ )	Amplitude (mV)	Rate ( $\text{s}^{-1}$ )	Charge ( $\text{n pe}^{-}$ )	Amplitude (mV)
–40	277	2.9	–198	162	2.3	–197
–60	250	3.0	–206	200	2.4	–205
–100	186	3.5	–238	171	2.7	–228
–150	88	5.8	–340	92	3.8	–294
–200	39	10.2	–518	47	6.0	–404
–300	20	15.0	–718	16	11.7	–655
–500	9	22.8	–1045	6	19.0	–1009

counting rates and charges obtained for different levels of discrimination are given in Table 1 for sequences of 10 000 pulses. It can be seen that for the lowest discrimination levels, counting rates and charges remains unchanged with discrimination levels, with a charge close to 1 photoelectron, which indicates that the main parts of dark pulses are close to real single photoelectron signals and that these two kind of signals cannot be distinguished. The counting rate for these pulses is around  $100 \text{ s}^{-1}$  for both PMs, which is comparable to the frequency of particles expected (around  $100 \text{ muons m}^{-2} \text{ s}^{-1}$ ). Special attention will have to be paid on eliminating contribution of these dark counts by either using high discrimination levels or using coincidence effects between different PMs. When the discrimination level amplitude is above the single photoelectron discrimination level, events with high amplitude still happen but with very low frequency of a few events per second.

## 2.3. Detection planes

The PM is now placed in its holder and in contact via the silicon interface disk to the wavelength shifting bar glued on the scintillator and is lighted by the light coupled to the shifting bar when muons strike the scintillating plate. The pulses are acquired for different discrimination levels with a view to analyze their characteristics in comparison to dark noise pulses. Assuming a flow of muons of  $100 \text{ m}^{-2} \text{ s}^{-1}$  [11,12], the expected rate on the plate is about  $12 \text{ s}^{-1}$ . The counting rates and mean charges for all sequence measurements are given in Table 2 for the different discrimination levels. At the lowest discrimination levels, pulses have mean charges from 2 to 5 photoelectrons and rate between 100 and  $300 \text{ s}^{-1}$ . This rate is higher than the sum of dark noise and expected muons events and shows in fact parasitic light from

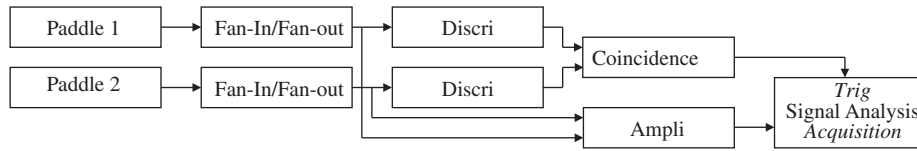


Fig. 3. Muon telescope coincidence calibration setup.

outside the plate. The mean charge is then the average charge for muon events but also for dark count and parasitic photonic events. When the amplitude of discrimination level is higher, only the highest amplitude events remain and the main part of single photoelectron events are suppressed. For discrimination values between 300 and 500 mV, the mean charge per event is between 10 and 20 photoelectrons, noise pulses are completely removed, the counting rate is consistent with the expected one and the observed events can be attributed to only muon events.

#### 2.4. Coincidence results

After having characterized the individual behaviour of both plates, the coincidence between the two plates can be investigated. The coincidence aims to provide a trigger signal when a muon runs through both plates. To study the characteristics of coincident signals, we use a setup made of two different circuits as represented in Fig. 3. The pulses out of the two PMs are copied by a fan-in fan-out module at the inputs of these two different circuits. In the first circuit, the pulses are discriminated and put in coincidence by a CAEN N455 NIM 'and' function unit to generate a logical trig signal. In the second circuit, the two PM outputs are amplified, acquired and statistically processed by the oscilloscope, the oscilloscope being triggered with signals generated by the first circuit. Based on the study of individual behaviour of both paddles, discrimination levels of the first circuit have been chosen to  $-100$  mV on the observed amplified signal. This discrimination level allows rejection of a large part of the single photoelectron noise while being confident not to reject real muon events. A typical signal after amplification showing the two PM outputs in coincidence is shown in Fig. 4.

A 100 000 signal acquisition has been carried out simultaneously on both paddle PM outputs when events are triggered by the logical coincidence signal. The correlated charge distribution which represents the charge simultaneously obtained on the two PMs output and which gives information on coincidence possibilities is shown in Fig. 5. It can be seen that the 1 photoelectron lines (the lines where charge for each plate is less than 1 photoelectron) are empty, which clearly indicates that noise signal has been removed. The charge distribution is very broad and extend to more than 10 photoelectrons. The histogram is also slightly dissymmetrical with respect to the diagonal line of equal charge for the two PMs, which may be the consequence of a better quality of paddle 1. The average rate of the observed events in coincidence is  $13.76 \text{ s}^{-1}$ , which is as expected. It is obtained when detection plates are as close as 3.5 cm. Note that when the distance between the plates is changed to 15, 30 and 60 cm, the counting rate is, respectively, changed to 10.3, 6.5 and  $2.6 \text{ s}^{-1}$ . It can be observed that for these 100 000 coincident signals, the number of events presenting a simultaneous charge, respectively, higher than 1, 2, 5, 10 photoelectrons on each of the paddles at the same time is, respectively, 99 927 (99.93%), 96 845 (96.85%), 81 974 (81.97%), and 48 243 (48.24%).

More than 99.9% of the detected events have more than 1 photoelectron simultaneously on both plates. Considering that

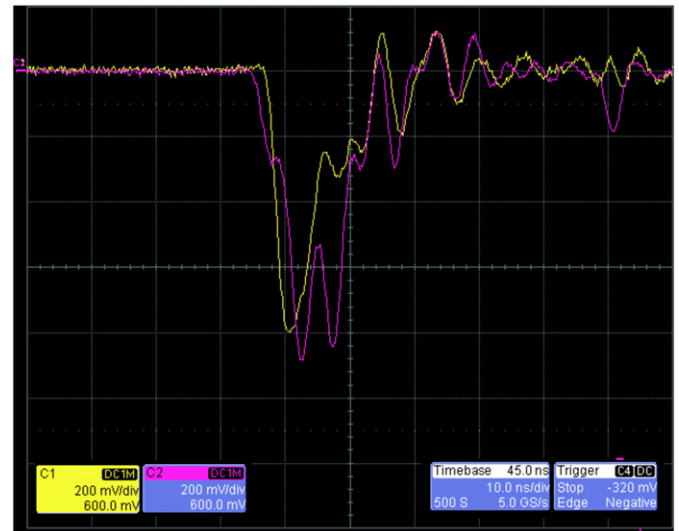


Fig. 4. Typical coincidence output signals of the two paddles.

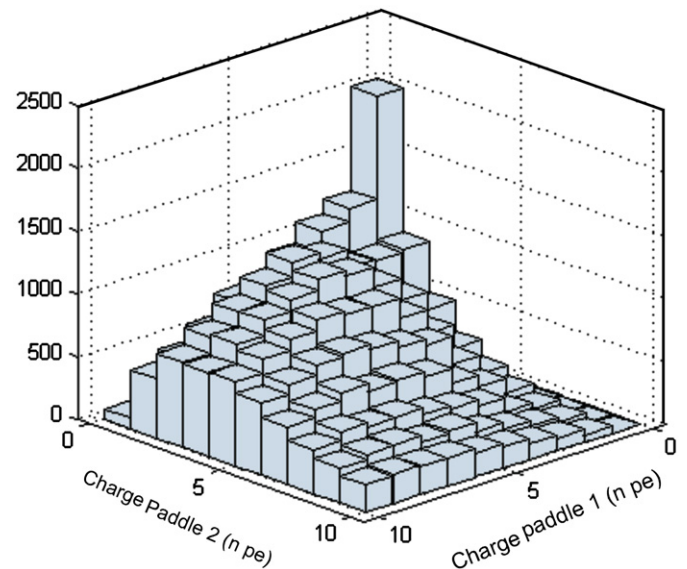


Fig. 5. Histogram representing simultaneous charge distribution on both paddles of the telescope in response to atmospheric muons. Horizontal axes are charges on each PM outputs given in number of photoelectrons generated at the photocathode level.

these signals are real muons, the detection efficiency of the telescope would be as high as 99.9%. It is, however, possible that a part of these signals are noise signals generated by residual parasitic light and the signal to noise ratio of the telescope can finally be confidently taken to 99%.



### 3. Photomultiplier tubes

In that part of the paper we present results related to the calibration of the PMs used in our scintillator detector. The anodes of the PMs will be coupled to optical fibers receiving light from the scintillator material. Before using it, this PM needs to be calibrated. We are especially interested in determining the gain of the different anodes of the PM. The gain allows associating the charge of an output signal to a corresponding number of photoelectrons produced at the photocathode level.

#### 3.1. The Hamamatsu multianode PM

The PMs used are  $4 \times 4$  multianode Hamamatsu R7600-00-M16. Such PMs or PMs of the same family have successfully been tested in large numbers in different experiences such as COMPASS RICH [13], EUSO [14], AMS RICH [15], Pamela [16], LHCb Rich [17], and even in similar fiber-reading configurations such as in MINOS [18,19,5], LHCb scintillator pad detector [6], ATLAS [20] or OPERA [21]. In all these experiments the PMs have generally demonstrated their reliability especially concerning effects of magnetic field, dark current, ageing, high voltage, single photoelectron detection efficiency, uniformity of gain and collection efficiency of individual anodes, cross-talk among all channels, linearity of response and operational stability of all tubes. For all these experiences, the choice of these photodetectors is mainly based on the reliability of all these parameters but also on geometry. An other interesting point is that such PMs have proved to be relevant to use in space applications [22,16].

#### 3.2. Choice of the discrimination level

In our tests, the PMs are used equipped with the standard voltage divider circuit proposed by Hamamatsu. They are powered in a negative polarity mode with high voltage value of  $-800$  V. Calibration has been performed for all the 16 pixels of the PM by lighting them at very low level so that the output is in the single photoelectron regime as described in Section 2.2. The observed signals are output of PM pixels through a  $50 \Omega$  load resistor that are then  $20 \times$  amplified, then discriminated before

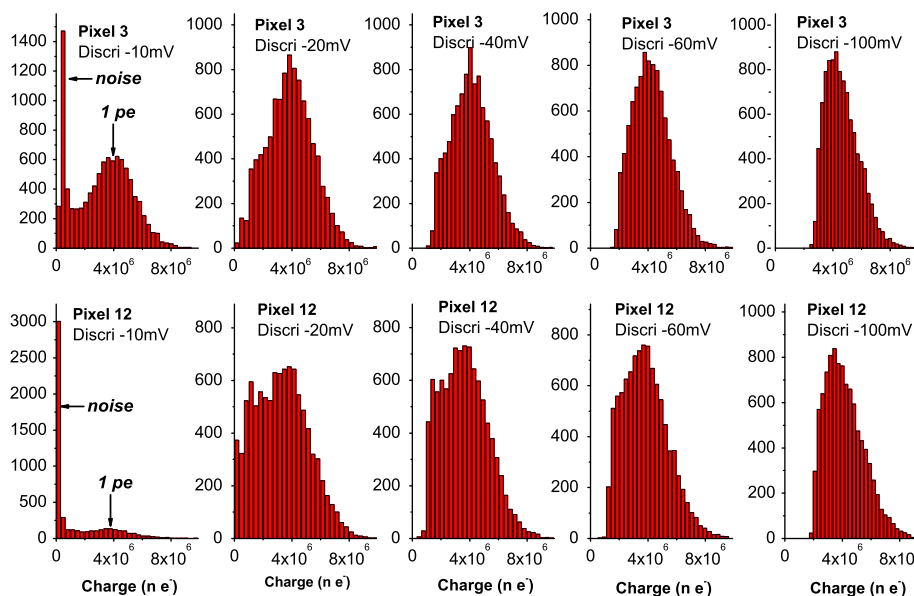
acquisition and finally statistically processed. Discrimination allows to select signal that have amplitude above the selected level and so acts as a filter to separate real signals from noise signals. The discrimination level must be carefully chosen in the acquisition process. If it is too low there will be a large number of noise signals, which will prevent a good statistics on real signals; if it is too high, a part of real signals with low amplitude may be eliminated and the results of the statistics will be biased. The discrimination level may be different for all pixels because pixels have different gains and different noise.

Fig. 6 shows charge histograms represented in number of electrical charges obtained for 10 000 single photoelectron pulses for two pixels for different discrimination levels. It can be seen that these two pixels have very different behaviours. At the lowest discrimination level, pixel 3 shows very clear Gaussian shape with pedestal around 0 resulting from all parasitic and noise signals whereas this shape is less clear for pixel 12. This difference is the result of a more important electrical noise for pixel 12. We observe that when the amplitude of the discrimination level is higher, the Gaussian shape is distorted in the low charge part of the spectrum, which is the consequence of filtering of real pulses.

#### 3.3. Single photoelectron response

For a good choice of the discrimination level, the obtained charge histogram is made of a clear Gaussian shape for the single photoelectron response with a pedestal for noise not as high as this single photoelectron Gaussian contribution. The gain is then evaluated by the mean number of electrons generated by pulse which is given by the center of the single photoelectron Gaussian shape. Charge histograms of the 16 pixels obtained after determination of the discrimination level are shown in Fig. 7. The corresponding discrimination levels and the obtained gain values are given for each pixel on the figure. It can be observed that the gain values are in agreement with typical value given by Hamamatsu of  $3.5 \times 10^6$ . It can also be seen that pixels show large disparity in gain values.

Complementary to these charge measurements, it is interesting to investigate amplitude characteristics, and especially to investigate the correlation between amplitude and charge and a possible equivalence between charge and amplitude. Amplitude is furthermore an important parameter because voltage is the



**Fig. 6.** Histogram representing the charge distribution of pixels 3 and 12 of the R5900 PM for different discrimination levels. The charge is given in number of electrons in the pulse.

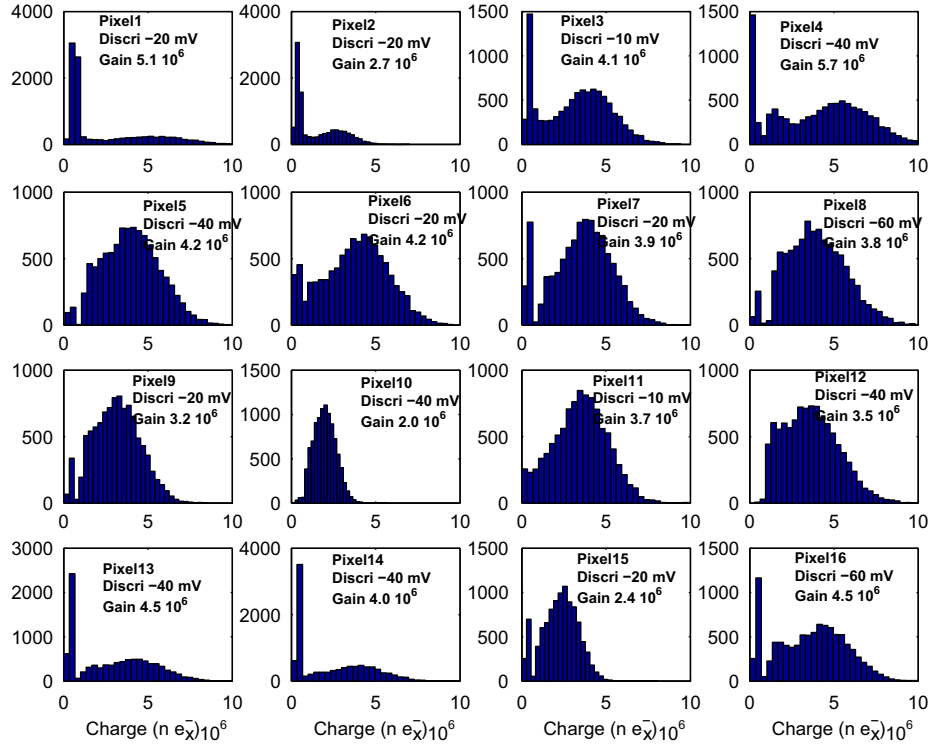


Fig. 7. Histogram representing the single photoelectron charge distribution of the 16 pixels of the R5900 PM. The charges are given in number of electrons in the pulse.

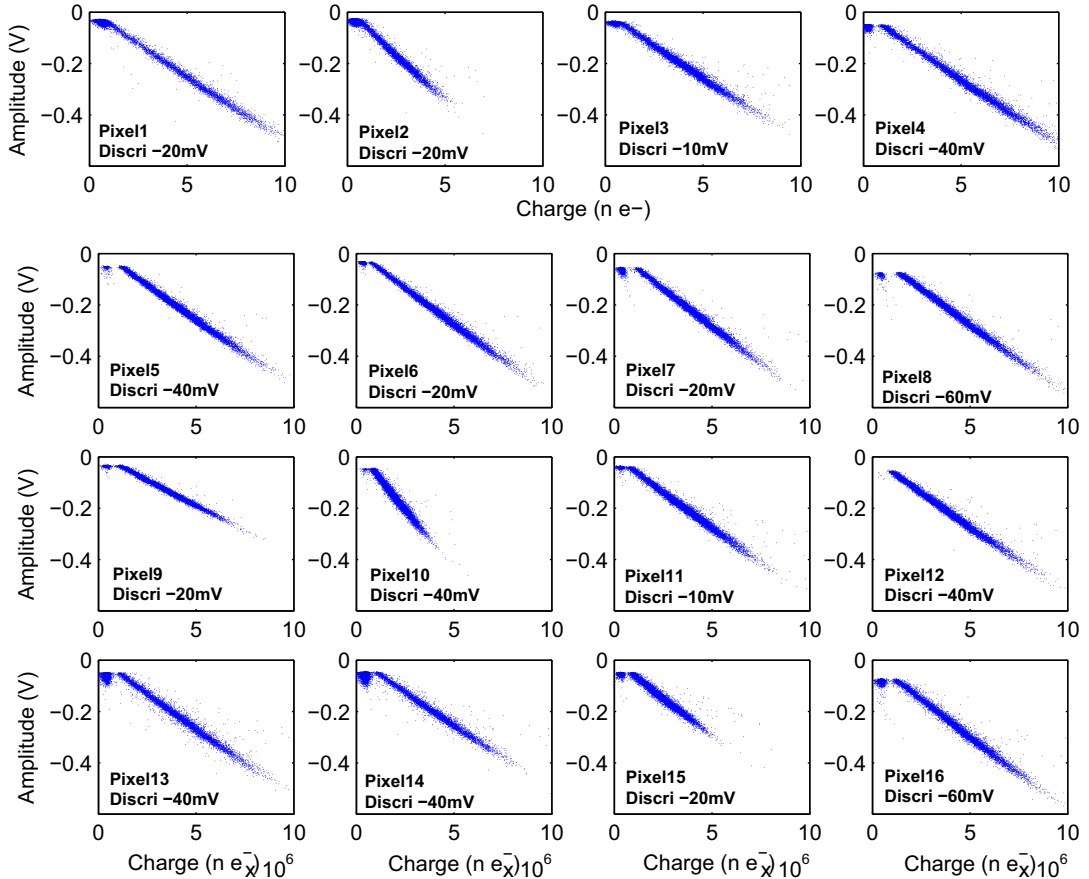


Fig. 8. Charge (in number of electrons) versus amplitude for 100 000 single photoelectron signals of the 16 pixels of the R5900 PM.

observable directly accessible in experimental setups. To evaluate this, a map of amplitude ( $V$ ) versus charge ( $C$ ) of all 10 000 signals is plotted for all 16 pixels in Fig. 8. A linear relationship can be observed between charge and amplitude except in the part of the low charge which can be attributed to noise contributions. This shows that the ratio between charge and amplitude is almost constant, which indicates that discrimination on amplitude and discrimination on charge are equivalent.

#### 4. Prototype preparation and results

The charged particle detection systems under investigation are the parts of the Simbol-X anticoincidence detector. The schematic view of a top part of the device is shown in Fig. 2 between the two stages of the muon telescope. We present here results obtained on a sample specifically prepared of such active shielding using previously studied multianode Hamamatsu R7600-00-M16 PM. Details about the elaboration process of the sample and then results concerning the response to atmospheric muons and to protons are given.

##### 4.1. Prototype preparation

The prototype sample of the anticoincidence detector is made of a  $8 \times 11 \times 1 \text{ cm}^3$  Saint-Gobain BC400 scintillator plate in which grooves are machined. The sample is shown in Fig. 9. Kuraray Y11 wavelength-shifting optical fibers are glued with Saint-Gobain BC600 space qualified optical glue in the grooves and are linked at the other end to a multianode PM. Eight grooves separated by 1 cm are machined along the long direction of the scintillator plate. The emission peak of the scintillator is around 425 nm and well matches the absorption spectrum of the waveshifting fibers which shifts this wavelength to a 475–490 nm range. The fibers collect a fraction of light emitted when a particle goes through the scintillator and guide it to the PM which changes the photonic incoming flux into an electrical signal.

The grooves are 2 mm deep and 1.2 mm wide machined according to standard plastics machining and polishing techniques. After cleaning of the different parts, the BC600 glue is deposited into the grooves. The fiber is then applied into the groove slowly from one end of the plate gradually to the other, paying special attention not to create air bubbles. Pieces of polycarbonate tubes are inserted 3 mm deep into the scintillator and the fibers threaded into protect them against breaking at the edge of the scintillator. The fibers are finally threaded into Hytrel jackets for protection (Fig. 9, left). Before they reach the PM, the fibers are gathered into two groups of four fibers in a specifically designed plastic tip (Fig. 9, middle). The tip is then mechanically linked to the PM assembly by a connector which makes the link between fiber ends and the PM entrance window thanks to a Saint-Gobain BC 634-A silicone optical interface slice (Fig. 9,

right). Finally one pixel is connected to four fibers. In this study the pixels 9 and 10 of the multianode PM have been used, one pixel for the four fibers of the right part of the plate and the other pixel for the four left fibers of the plate. Detection performances of this sample have then been evaluated under illumination of muons thanks to the previously described muon telescope and under illumination of  $\sim 15\text{--}20 \text{ MeV}$  protons.

##### 4.2. Muons response

The plate to be tested is inserted between the two stages of the muon telescope. The distance between the two detection areas of the telescope is 3.5 cm, which corresponds to a particle counting rate of  $13 \text{ s}^{-1}$ . A trig signal is emitted when a muon runs through both stages of the telescope. However, because the detection areas of the telescope plates are larger than the tested plate it can be estimated by considering simple surface ratio that only 7.2% of the particles running through the telescope will also run through the test plate and create a significant simultaneous signal on the two pixels, the other events resulting in a useless zero contribution. We have carried out a 180 000 events data acquisition with the telescope described in Section 2. The average rate of events detected by the telescope is  $13.26 \text{ s}^{-1}$  for 180 000 events. Considering the coincidence behaviour of the two parts of the plate, it can be observed that for these 180 000 coincident signals, the number of events presenting a simultaneous charge, respectively, higher than 1, 2, 5, 10 photoelectrons on each of the paddles at the same time is, respectively, 13 518 (7.51%), 13 066 (7.26%), 10 358 (5.85%), and 4914 (2.73%). Assuming that events presenting simultaneous charge higher than 1 photoelectron on the two pixels are real muons events, 7.5% of events triggered by the telescope can be considered as real events that run through the telescope and the tested plate at the same time, which is as expected.

Histograms of charge distribution of these 13 518 events for each of the pixels are shown in Fig. 10. The average charge of these 13 518 events is 12.6 photoelectrons and 10.1 photoelectrons, respectively, for pixels 9 and 10. Because events that present a charge less than 1 photoelectron on either pixels have been rejected, the 0–1 photoelectron signal is 0. However, the histogram curve trend seems to tend with regular decay to a non-zero value but to a value around 50. These possible 50 real events on each pixel that have been rejected (100 events in total out of 13 518) make a possible error of less than 1% or a possible detection efficiency higher than 99%. This good detection efficiency needs to be regarded as a worst case rough estimate, it can be more precisely given by focusing on low level signals which should be the subject of a next study. It should be noticed that this test has been performed in difficult conditions with large amount of wrong events and noise (especially electrical noise and parasitic light noise). In spite of this, the tested plate has shown very good detection efficiency and also very good ability to reject

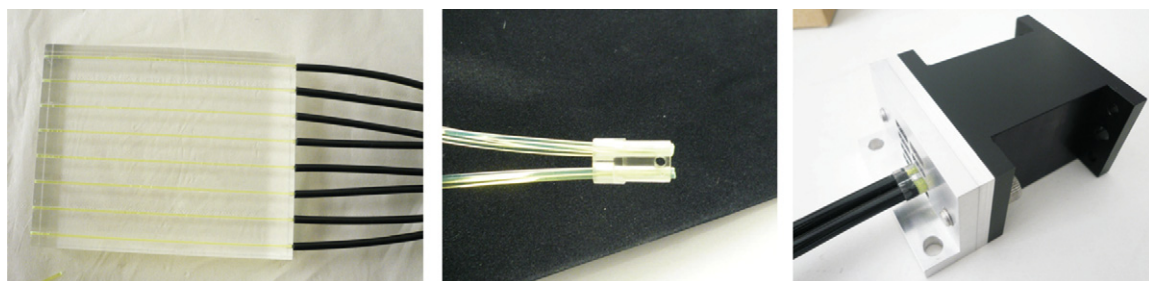


**Fig. 9.** View of sample prototype of active shielding: fibers glued into grooves and jacketed into Hytrel tubes (left), fibers gathering and connection tip (middle) and connection to the PM assembly.

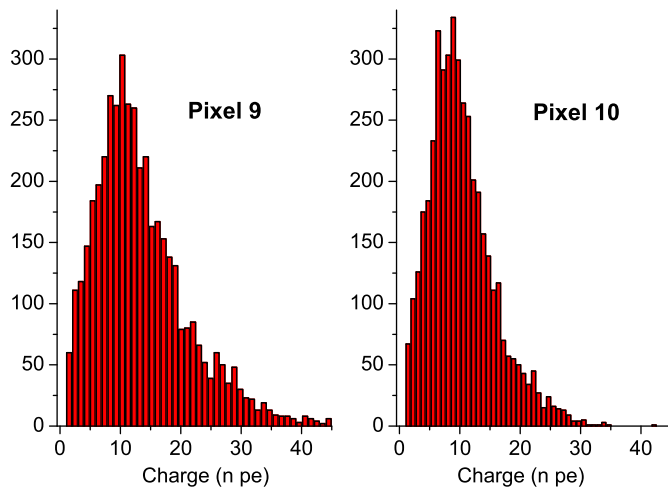


**Fig. 10.** Histograms representing charge distribution of both parts of the active shielding sample in response to atmospheric muons. The charge is given in number of generated photoelectrons.

wrong events. There is no doubt that the detection efficiency can be largely improved by (i) reducing parasitical ambient light thanks to a better isolation of light sensitive components, (ii) improving quality of electrical signals out of PM by isolating against electrical parasitic signals, (iii) use of coincidence between two or more pixels.

#### 4.3. Protons response

The response of the plate has been evaluated under excitation of protons at IPN-Orsay (Institut de Physique Nucléaire d'Orsay). The proton source is a  $\sim 15$ – $20$  MeV beam scattered on a gold target. The tested plate is placed inside an aluminum holder with beam aperture of 50 mm diameter. It is placed inside a chamber 50 cm away from the gold target with a scattering angle of  $\sim 10^\circ$ . Results are presented for a  $1\ \mu\text{m}$  thick gold target. This time the arrival of particles is not triggered; the device needs to detect particles its own way. Because of experience geometry the tested device was not completely isolated against ambient light and the PMs have received a strong continuous ambient parasitic light. To minimize the effects of this parasitic light, after different measurement configuration tests concerning the detection mode (pixels in coincidence or not) and choice of detection levels, it has been chosen to perform the test with the two pixels in coincidence. The discrimination level for the two pixels after amplification has been chosen to  $-200$  mV. These levels are relatively high to filter effects of parasitic light and it can be thought that events with low signal will be rejected.

For 50 000 consecutive events, detected with an average rate of  $8667\ \text{s}^{-1}$ . Considering the coincidence behaviour of the two parts of the plate, it can be observed that for these 180 000 coincident signals, the number of events presenting a simultaneous charge, respectively, higher than 1, 2, 5, 10, 20, 50 photoelectrons on each of the paddles at the same time is, respectively, 49 992 (99.98%), 49 984 (99.97%), 49 674 (99.35%), 45 931 (91.86%), 5372 (10.74%), and 1 (0.002%). The histogram presenting the charge distribution obtained on each of the pixels for these 50 000 events is shown in Fig. 11. The average simultaneous charge is 20.1 photoelectrons and 18.4 photoelectrons, respectively, for pixels 9 and 10. Protons produce a signal that can easily be detected. The signal is, however, a little bit low in comparison to the deposited energy. Using the NIST ("National Institute of Standard and Technology")

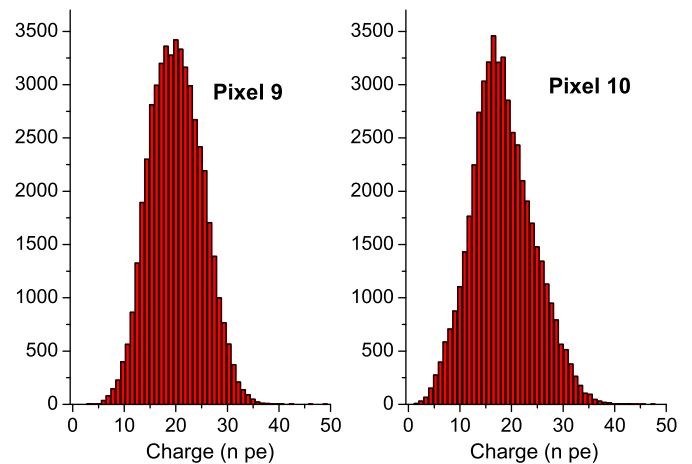


**Fig. 11.** Histograms representing charge distribution of both parts of the active shielding sample in response to 15 MeV protons. The charge is given in number of generated photoelectrons.

database for the range of protons in plastic, it can be calculated that 15 MeV protons deposit all their energy in the few top millimetres of the plate whereas  $\sim 1$  GeV muons deposit only approximately 2 MeV, but the protons resulting signal is only two times stronger than the muon one. This may be explained by the fact that light produced by the protons is generated in the top few millimetres of the plate whereas the light produced by the muons is generated along the whole thickness of the plate and the light is not coupled the same way in both cases. This suggests that coupling of light is more efficient when the light is produced along the whole thickness of the plate. This is an interesting point that needs to be clearly understood by the help of optical simulations.

#### 5. Conclusion

The fabrication process and performance evaluation of a prototype piece of active shielding usable in the anticoincidence detector of the Simbol-X mission has been presented. This piece of detector is made of plastic scintillator in which waveshifting fibers are inserted and connected for light detection to multi-anode PMs. To test the response of this device, a muon telescope has been developed. The muon telescope consists in two scintillator stages coupled to PMs thanks to waveshifting bars. It can detect muons with great confidence. The device has also been tested with 15 MeV protons at the IPN-Orsay. The average number of detected photoelectrons is around 10 and 20, respectively, for these two sources of particles, which allows a very efficient detection. What is more, in spite of difficult and especially noisy conditions, the device has shown a very good ability to reject noise events. In short this design has two advantages: good detection efficiency and good noise rejection.

Although this detection technology shows good performances, improvements can be made by reducing noise and improving some technological aspects and so improve the detection threshold. Two main noise sources arise from the tested plate: electrical noise of the PM due to bad electrical isolation to parasitic signal, and optical noise due to parasitic light that comes into the device and produce wrong signals at the PM level because of bad isolation to external light. These noise sources need to be investigated in more details and removed. Coincidence between pixels has also revealed a great ability to reduce wrong events, which is an other way to reduce the noise. Similar noise problems



also affect the performances of the test equipments that can also be improved to have again more accurate characterization tools.

Some technical aspects can also be investigated to improve intrinsic detection performances of the active shielding. Wrapping the devices facilitates internal reflections of light and so improves coupling efficiency of light into the fibers. Adding reflective materials or metallization of the free end of the fibers allows to redirect to the PMs a part of the photons that have been coupled in the wrong direction. In addition, results concerning protons depositing their energy in the few top millimetres have suggested the coupling efficiency of light in the fibers depends on the position where the photons are emitted. A complete understanding of the coupling mechanisms of light based on simulations would help improving collecting light. A paper concerning these aspects is under preparation by our group. Finally, it should also been noticed that vibration resistance tests have been performed; the response of the device is not altered after vibrations, which is a necessary condition for space applications.

## References

- [1] J. Rodriguez, P. Ferrando (Eds.), *Simbol-X: Focusing on the Hard X-Ray Universe: Proceedings of the 2nd International Simbol-X Symposium*, vol. 1126, AIP, 2009.
- [2] R. Wojcik, B. Kross, S. Majewski, A. Weisenberger, C. Zorn, *Nucl. Instr. and Meth. A* 342 (1994) 416.
- [3] Y.K. Lee, R. Debye, J.H. Lee, H. Ito, S.J. Sanders, *Nucl. Instr. and Meth. A* 516 (2004) 281.
- [4] A. Weisenberger, A. Day, B. Kross, S. Majewski, R. Wojcik, C. Zorn, *Nucl. Instr. and Meth. A* 327 (1993) 500.
- [5] N. Tagg, A. de Santo, A. Weber, A. Cabrera, P.S. Miyagawa, M.A. Barker, K. Lang, D. Michael, R. Saakyan, J. Thomas, *Nucl. Instr. and Meth. A* 539 (2005) 668.
- [6] E. Aguilo, R. Ballabriga, A. Comerma, L. Garrido, D. Gascón, R. Graciani, E. Graugés, X. Vilasis-Cardona, X. Xirgu, G. Böhner, R. Bonnefoy, D. Borrás, R. Cornat, M. Crouau, O. Deschamps, P. Jacquet, J. Lecoq, S. Monteil, P. Perret, G. Reinmuth, *Nucl. Instr. and Meth. A* 538 (2005) 255.
- [7] B. Abbott, R. Davies, D. Koltick, R. McIlwain, C. Schmitz, E. Shibata, M. Atac, B. Baumbaugh, J. Jaques, R. Kehoe, J. Marchant, R. Ruchti, J. Warchol, M. Wayne, M. Binkley, J. Elias, H. Goldberg, S. Margulies, J. Solomon, T. Armstrong, R. Lewis, G. Smith, *Nucl. Instr. and Meth. A* 327 (1993) 319.
- [8] A. Moiseev, P. Deering, R. Hartman, T. Johnson, T. Nebel, J. Ormes, D. Thompson, *Nucl. Instr. and Meth. A* 583 (2007) 372.
- [9] A. Moiseev, R. Hartman, J. Ormes, D. Thompson, M. Amato, T. Johnson, K. Segal, D. Sheppard, *Astropart. Phys.* 27 (2007) 339.
- [10] F. Perotti, M. Fiorini, S. Incorvaia, E. Mattaini, E. Sant'Ambrogio, *Nucl. Instr. and Meth. A* 556 (2006) 228.
- [11] H. Geenen, AMANDA Collaboration, Atmospheric neutrino and muon spectra measured with the AMANDA-II detector, in: *International Cosmic Ray Conference, International Cosmic Ray Conference*, vol. 3, p. 1313.
- [12] S.A. Minnick, A.S. Beach, J.J. Beatty, A. Bhattacharyya, C.R. Bower, S. Coutu, M.A. Duvernois, A.W. Labrador, S.P. McKee, D. Mueller, J.A. Musser, S.L. Nutter, M. Schnubnell, S.P. Swordy, G. Tarle, A.D. Tomasch, Energy spectra and charge ratios of atmospheric muons, in: *International Cosmic Ray Conference, International Cosmic Ray Conference*, vol. 3, p. 1191.
- [13] P. Abbon, M. Alexeev, H. Angerer, R. Birska, P. Bordalo, F. Bradamante, A. Bressan, M. Chiosso, P. Ciliberti, M. Colantoni, T. Dafni, S. Dalla Torre, E. Delagnes, O. Denisov, H. Deschamps, V. Diaz, N. Dibiase, V. Duic, W. Eyrich, A. Ferrero, M. Finger, M. Finger Jr., H. Fischer, S. Gerassimov, M. Giorgi, B. Gobbo, R. Hagemann, D. von Harrach, F. Heinsius, R. Joosten, B. Ketzer, V. Kolosov, K. Königsmann, I. Konorov, D. Kramer, F. Kunne, A. Lehmann, S. Levorato, A. Maggiora, A. Magnon, A. Mann, A. Martin, G. Menon, A. Mutter, O. Nähle, F. Nerling, D. Neyret, D. Panzieri, S. Paul, G. Pesaro, C. Pizzolotto, J. Polak, P. Rebourgeard, F. Robinet, E. Rocco, P. Schiavon, C. Schill, P. Schoenmeier, W. Schroeder, L. Silva, M. Slunecka, F. Sozzi, L. Steiger, M. Sulc, M. Svec, S. Takekawa, F. Tessarotto, A. Teufel, H. Wollny, *Nucl. Instr. and Meth. A* 595 (2008) 177. RICH 2007—Proceedings of the Sixth International Workshop on Ring Imaging Cherenkov Detectors.
- [14] N. Inoue, S. Hasegawa, Y. Walda, MAPMT ageing tests for high-intensity incident lights and high voltage switching, in: *International Cosmic Ray Conference, International Cosmic Ray Conference*, vol. 8, p. 145.
- [15] M. Buénerd, *Nucl. Instr. and Meth. A* 502 (2003) 158.
- [16] G. Barbarino, M. Boscherini, D. Campana, G. De Rosa, W. Färnkranz, W. Menn, G. Osteria, G. Passeggi, R. Rocco, S. Russo, M. Simon, E. Vanzanella, *Nucl. Instr. and Meth. A* 584 (2008) 319.
- [17] E. Albrecht, J. Baker, G. Barber, J. Bibby, M. Calvi, M. Charles, A. Duane, S. Easo, S. Eisenhardt, L. Eklund, M. French, V. Gibson, A. Halley, R. Halsall, N. Harnew, M.J.J. John, S.G. Katvars, J. Libby, F. Muheim, M. Paganoni, A. Petrolini, S. Playfer, D. Price, J. Rademacker, N. Smale, S. Topp-Jorgenson, D. Websdale, G. Wilkinson, S.A. Wotton, *Nucl. Instr. and Meth. A* 488 (2002) 110.
- [18] K. Lang, J. Day, S. Eilerts, S. Fuqua, A. Guillen, M. Kordosky, M. Lang, J. Liu, W. Opaska, M. Proga, P. Vahle, A. Winbow, G. Drake, J. Thomas, C. Andreopoulos, N. Saoulidou, P. Stamoulis, G. Tzanakos, M. Zois, A. Weber, D. Michael, *Nucl. Instr. and Meth. A* 545 (2005) 852.
- [19] K. Lang, J. Day, S. Eilerts, S. Fuqua, M. Kordosky, P.L. Vahle, P. Dervan, R. Saakyan, J. Thomas, M. Barker, P.S. Miyagawa, A. De Santo, A. Weber, G. Tzanakos, H. Kim, D. Michael, M. Ignatenko, V. Makeev, A. Para, R. Lee, C. Bower, S. Mufson, P. Border, P. Cushman, K. Ruddick, R. Schwienhorst, P. Adamson, P.G. Harris, R.C. Webb, W. Oliver, J. Schneps, *Nucl. Instr. and Meth. A* 461 (2001) 571.
- [20] S. Ask, P. Barrillon, A. Braem, C. Cheiklali, I. Efthymiopoulos, D. Fournier, C. de La Taille, B. di Girolamo, P. Grafstrom, C. Joram, M. Haguenaue, V. Hedberg, B. Lavigne, A. Maio, A. Mapelli, U. Mjörnmark, P. Puzo, M. Rijssenbeek, J. Santos, J.G. Saraiva, H. Stenzel, M. Thioye, E. Valladolid, V. Vorobel, *Nucl. Instr. and Meth. A* 568 (2006) 588.
- [21] E. Baussan, K. Borer, J.-E. Campagne, N. Chon-Sen, M. Dracos, Y. Gornushkin, J.-L. Guyonnet, J.J. Csathy, C. Jollet, F. Juget, A. Krasnoperov, Z. Krumstein, U. Moser, A. Nozdrin, A. Olchevski, A. Sadovski, P. Vilain, T. Wälchli, G. Wilquet, *Nucl. Instr. and Meth. A* 581 (2007) 465.
- [22] K. Rielage, K. Arisaka, M. Atac, W.R. Binns, M.J. Christl, P. Dowkontt, J.W. Epstein, P.L. Hink, M.H. Israel, D. Leopold, G.N. Pendleton, D.B. Wallace, *Nucl. Instr. and Meth. A* 463 (2001) 149.